nature COMMUNICATIONS

ARTICLE

DOI: 10.1038/s41467-018-07204-y OPEN

Myths and reality of $HPbI_3$ in halide perovskite solar cells

Weijun Ke[1], Ioannis Spanopoulos[1], Constantinos C. Stoumpos[1] & Mercouri G. Kanatzidis[1]

All-inorganic perovskites have a special place in halide perovskite family because of their potential for better stability. However, the representative cesium lead iodide ($CsPbI_3$) is metastable and spontaneously converts to the non-perovskite structure at room temperature. Here, we demonstrate that what appears to be all-inorganic $CsPbI_3$ stabilized in its perovskite form using the purported intermediate known as hydrogen lead iodide ($HPbI_3$) is, in fact, the hybrid perovskite cesium dimethylammonium lead iodide ($Cs_{1-x}DMA_xPbI_3$, $x = 0.2$ to 0.5). Thus, many of the reported all-inorganic perovskites are actually still hybrid organic-inorganic perovskites, as strongly evidenced by a wide battery of experimental techniques presented here. Solar cells based on the representative composition $Cs_{0.7}DMA_{0.3}PbI_3$ can achieve an average power conversion efficiency of 9.27 ± 1.28% (max 12.62%). These results provide an alternative angle to look at previous results pertaining all-inorganic $CsPbI_3$ while the DMA cation is now revealed as an alternative A site cation.

[1] Department of Chemistry, Northwestern University, Evanston, IL 60208, USA. Correspondence and requests for materials should be addressed to C.C.S. (email: konstantinnos.stoumpos@northwestern.edu) or to M.G.K. (email: m-kanatzidis@northwestern.edu)

Halide perovskites have unique properties such as tunable band gaps, long diffusion lengths, high optical absorption coefficients, and low exciton binding energies[1–8]. Halide perovskite solar cells have achieved a record power conversion efficiency (PCE) of 22.7%[9], which are a great candidate for the next generation of photovoltaics. High-performance perovskite solar cells typically employ organic-inorganic hybrid Pb-based perovskites as light absorbers such as methylammonium lead iodide ($MAPbI_3$), formamidinium lead iodide ($FAPbI_3$), and their mixtures, due to their excellent optical and electrical properties[10–16]. However, the intrinsic thermal and light instabilities of organic cations of MA and FA present serious hurdles in the further development and commercialization of long-term operating devices[17]. The all-inorganic perovskite analog cesium lead iodide ($CsPbI_3$) could present an important way forward, since it possesses a relatively wider band gap with large band widths and especially a significantly better thermal stability compared with the organic cations-based perovskites[17–20]. However, the black $CsPbI_3$ perovskite is metastable and it spontaneously converts to the undesired yellow polytype (δ-phase, NH_4CdCl_3 structure-type) at room temperature[5,18,21,22]. Yellow δ-$CsPbI_3$ has a wide band gap of $E_g = 2.82$ eV and has poor transport properties[18]. By contrast, black $CsPbI_3$ has a narrow band gap of around 1.7 eV and it is suitable for solar cell applications[21,23]. Therefore, much effort has been devoted to improving the phase-stability of the black-phase $CsPbI_3$ perovskites so that highly efficient all-inorganic solar cells can be made[18,24–35]. In one approach, researchers used pre-synthesized $CsPbI_3$ nanocrystals to make solar cells. For example, Protesescu et al. demonstrated that the black $CsPbI_3$ perovskite (γ-phase) could be stabilized as nanocrystals[36], due to the large contribution of surface energy. Subsequent work by Luther et al. demonstrated that colloidal $CsPbI_3$ quantum dots synthesized by a hot-injection method can be phase-stable for several months in ambient air and the solar cells achieved a PCE as high as 13.43%[27,28]. In another approach, You et al. used dimethylformamide (DMF)/dimethyl sulfoxide (DMSO) solvent followed by high-temperature annealing process to obtain the black α-phase $CsPbI_3$[33]. These solar cells yielded a record PCE of 15.7% and showed a good light-soaking stability under the protection of N_2-filled glovebox. Much more commonly, the use of hydriodic acid (HI)[18,26] or the so-called hydrogen lead iodide ($HPbI_3$) precursor[31,37], produced by HI treatment, are the most used approaches to stabilize the black α-$CsPbI_3$. The use of $HPbI_3$ was first reported as an intermediate in the synthesis of $FAPbI_3$ solar cells[38], and was prepared by mixing PbI_2 and HI in DMF. Eperon et al. subsequently reported that HI can be used directly as an additive in DMF solutions of $CsPbI_3$ to stabilize the black α-$CsPbI_3$ films at room temperature[18]. The planar device made from this black $CsPbI_3$ film achieved a PCE of 2.9%. Recently, Zhang et al. reported the formation of black $CsPbI_3$ by a low-temperature deposition using the pre-synthesized PbI_2·xHI, which was also made from DMF, PbI_2, and HI[31]. Combined with the use of larger ethylenediammonium (*en*) cation, the champion α-$CsPbI_3$ solar cell yielded a PCE of 11.8% with enhanced stability and good reproducibility[31]. More recently, Jiang et al. also used $HPbX_3$ (X = I, Br) as the precursor together with phenylethylammonium (PEA) cation to fabricate low-dimensional α-$CsPbI_3$ and the solar cells achieved a high PCE of 12.4%[37]. Despite the apparent success of the $HPbI_3$ methodology, the mechanism of the stabilization of the black $CsPbI_3$ by HI and $HPbI_3$ remains unclear. The claim alone that $HPbI_3$ even exists is extraordinary and there is no structural or spectroscopic validation for the existence of this compound. From the chemistry point of view, $HPbI_3$ would be a solid acid with HI fragment in it and intuitively is unlikely to exist. This is because the HI molecule itself is not known to engage in binding to metals and it is likely that cannot form a stable structure[39] and will readily dissociate to PbI_2 and HI. Thus, the claim that $HPbI_3$ is a real compound deserves closer attention and we set out to investigate it in the context of the present manuscript.

Here, we report that $HPbI_3$ does not exist and instead what was believed to be it is in fact a compound of $DMAPbI_3$ (DMA = dimethylammonium, $(CH_3)_2NH_2^+$), where DMA is a decomposition product of the acidic hydrolysis of DMF catalyzed by HI. We demonstrate that the black $CsPbI_3$ films deposited from DMF containing HI/$HPbI_3$ and reported to be all-inorganic black phase of $CsPbI_3$ are not. Instead, they are the mixed-cation perovskite phase of cesium dimethylammonium lead iodide ($Cs_{1-x}DMA_xPbI_3$, $x = 0.2$ to 0.5). The α-$Cs_{1-x}DMA_xPbI_3$ perovskite films have similar characteristics with the black γ-$CsPbI_3$ films arising from HI addition, but they exhibit better charge transport due to the superior band structure characteristics (larger bandwidth, smaller band gap) of the cubic phase. Our best-performing solar cell based on α-$Cs_{0.7}DMA_{0.3}PbI_3$ perovskite absorber achieves a remarkable PCE of 12.62%. Our results reveal the existence of α-$Cs_{0.7}DMA_{0.3}PbI_3$ a black 3D perovskite which is a great absorber for the fabrication of high efficiency solar cells.

Results

Phase diversity of $CsPbI_3$. The structure of halide perovskites which have a general formula of AMX_3 can be only stabilized by limited cations, according to the rule of tolerance factor, t[39,40]. Where A, M, and X represent a nonbonding univalent cation, an octahedrally coordinated bivalent metal ion, and a monoanionic halide ion, respectively[5,41]. A cubic structure of perovskite materials typically has a suitable t value ranged from 0.9 to 1.0, which is defined by the equation of $t = (r_A + r_X)/\sqrt{2}(r_M + r_X)$. r_A, r_M, and r_X represent the ionic sizes of A, B, and X, respectively[42]. Different A cations have different ionic sizes, only cubic $MAPbI_3$ could be stable at room temperature. Both $FAPbI_3$ and $CsPbI_3$ normally adopt the yellow phase at room temperature, due to the too large and too small size of A cations, respectively[5,42]. Specifically, $CsPbI_3$ can adopt two structures:[21] the NH_4CdCl_3-type yellow phase (δ-phase) stable at room temperature (Fig. 1a) and the black cubic $CaTiO_3$-type (α-phase) structure stable above 300 °C (Fig. 1b). The perovskite structure can be kinetically stabilized at room temperature, where it adopts the black orthorhombic γ-phase (bandgap of around 1.73 eV) but it converts within hours to the δ-phase[5,42,43]. Thus, $CsPbI_3$ is typically stabilized by adjusting the t via formation of solid solutions such as partial replacement of I with smaller Br anions to form $CsPbI_{3-x}Br_x$ compositions, which exhibit a wider band gap[44–54], or by substituting the A-site with larger organic cations such as FA to form $Cs_{1-x}FA_xPbI_3$ solid solutions[55]. DMA (2.72 Å) is very similar in shape to FA (2.53 Å) but has a slightly larger effective radius owing to the conjugated bonding in the latter (Fig. 1c)[56,57]. Because of this, pure $DMAPbI_3$, which has a large $t = 1.026$ and is not able to form the perovskite structure, unlike $FAPbI_3$. Pure $DMAPbI_3$, which is identical to what previously reported as $HPbI_3$, by inspection of the reported and simulated powder diffraction patterns (PXRD), has a 1D structure assembled by face-sharing $[PbI_6]^{4-}$ octahedra[58], and it is isostructural with yellow $FAPbI_3$[5]. Unlike $FAPbI_3$, $DMAPbI_3$ cannot be isolated as a black perovskite due to the too large size of DMA which leads to a prohibitively large t, even at elevated temperatures. On the other hand, the effective radius of Cs cation is only 1.88 Å and pure $CsPbI_3$ has a low tolerance factor of $t = 0.851$ which is below the ideal range of cubic structure (Fig. 1d)[17,19]. However, mixing Cs with DMA, i.e., $Cs_{1-x}DMA_xPbI_3$, can on average bring the effective tolerance factor within the desirable region, thus enabling the stabilization of a black perovskite phase, namely

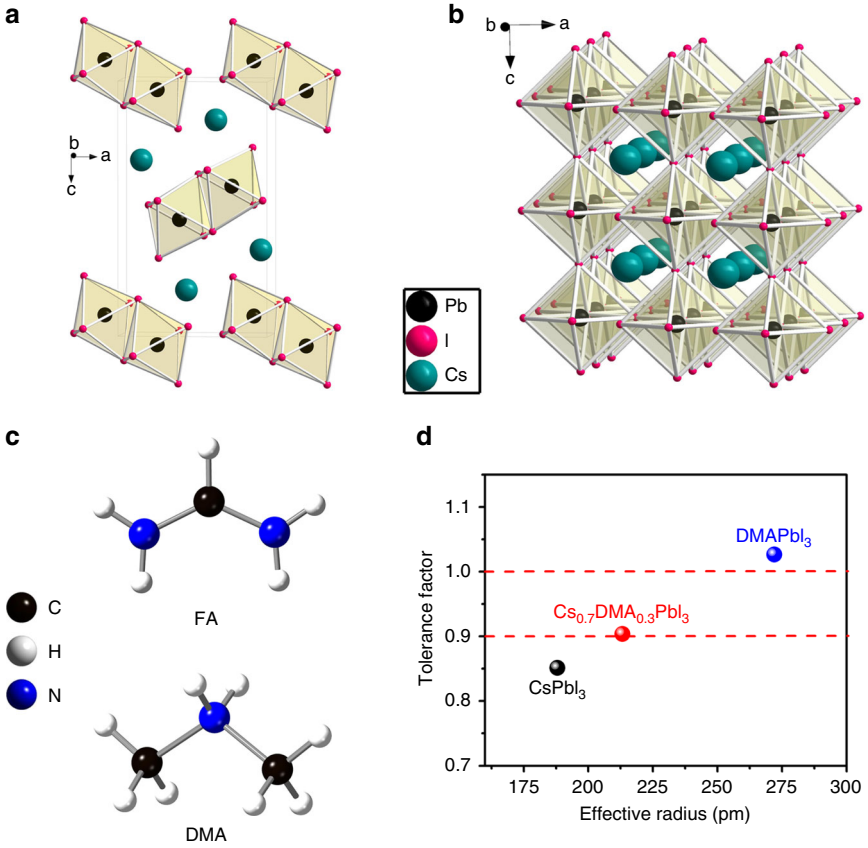

Fig. 1 Crystal and molecular structures. **a** Crystal structure of $CsPbI_3$ with non-perovskite yellow orthorhombic (δ) phase. **b** Crystal structure of $CsPbI_3$ with perovskite black cubic (α) phase. **c** Molecular structures of FA (top) and DMA (bottom) cations. **d** Tolerance factors of $CsPbI_3$, $DMAPbI_3$, and $Cs_{0.7}DMA_{0.3}PbI_3$

$Cs_{1-x}DMA_xPbI_3$ ($x = 0.2$ to 0.5), having a $t = 0.904$ ($x = 0.3$) that allows it to adopt the cubic α-phase (Fig. 1d), similarly to $Cs_{1-x}FA_xPbI_3$.

$Cs_{1-x}DMA_xPbI_3$ film properties. This has indeed turned out to be the case in our thin films, where the nominal $Cs_{0.7}DMA_{0.3}PbI_3$ composition is able to adopt the perovskite phase. As shown in Fig. 2a, the $Cs_{0.7}DMA_{0.3}PbI_3$ film without HI addition shows a black color, indicting the successful fabrication of black-phase perovskite structure with lattice constant $a = 6.272$ Å and *Pm*-3*m* space group. On the contrary, the pristine $CsPbI_3$ and $DMAPbI_3$ films deposited on FTO/PEDOT substrates are yellow and pale-yellow color (Fig. 2a), respectively, because they are non-perovskite NH_4CdCl_3 structure-type[56]. For comparison, we also fabricated $CsPbI_3$ film with HI addition (see details in Methods). Similar to the previously reported results[18,25,26,59], the $CsPbI_3$ film prepared with HI addition also shows a black color and a shiny surface (Fig. 2a), indicative of the formation of the similar black-phase perovskite structure. The color of the films is in good agreement with the band gaps of the respective compounds as determined by optical absorption measurements. Fig. 2b shows that the $Cs_{0.7}DMA_{0.3}PbI_3$ film has an absorbance onset at around 730 nm, indicating a band gap of 1.7 eV. The $CsPbI_3$ film with HI addition shows a similar absorption but slightly blue-shifted from 730 nm to 710 nm. As expected, the pure $CsPbI_3$ and $DMAPbI_3$ films only show an absorption at around 440 nm and 390 nm, respectively, due to the wide band gaps of these yellow phases[18]. Photoluminescence (PL) measurements reveal the same trend. As shown in Fig. 2c, the $Cs_{0.7}DMA_{0.3}PbI_3$ film has a PL emission at around 724 nm. The black $CsPbI_3$ film with HI addition shows a blue-shift PL peak at around 704 nm, consistent with the trend of UV-vis absorption spectra. Both $CsPbI_3$ and $DMAPbI_3$ films only show negligible PL emission, due to the indirect nature of the band gaps.

X-ray diffraction (XRD) patterns on the thin-films confirm the structure description discussed above. As shown in Fig. 2d, the main peaks of the neat yellow $CsPbI_3$ film locates at 9.9°, 13.2°, 22.8° etc. are assigned to the orthorhombic (*Pnma*) yellow δ-phase (Supplementary Fig. 1)[18]. The XRD pattern of the $DMAPbI_3$ film only shows two main reflections at $2\theta = 11.8°$ and 20.4° (Fig. 2d), due to the preferred orientation, corresponding to the hexagonal ($P6_3/mmc$) yellow phase (Supplementary Fig. 2). The $Cs_{0.7}DMA_{0.3}PbI_3$ film shows peaks at $2\theta = 14.4°$, 20.2°, 28.9°, and 40.9° etc., which can be indexed to the (100), (110), (200), and (220) reflections of cubic $CsPbI_3$, showing some orientation of the perovskite in both (100) and (110) directions of the cubic (*Pm*-3*m*) α-phase (Supplementary Fig. 3)[18,30]. While the $CsPbI_3$ film with HI additive exhibits similar peaks, it has no preferred orientation showing reflections that correspond to the black orthorhombic (*Pbnm*) perovskite γ-phase (Supplementary Figs. 4–5). In addition, the $CsPbI_3$ film with HI also reveals a weak reflection at $2\theta = 9.9°$, which corresponds to the yellow δ-phase, indicating that the conversion to the black phase is incomplete.

To further prove that DMA cation is actually present in the black $CsPbI_3$ films, we measured the proton nuclear magnetic resonance (^{1}H NMR) spectrum of the powder obtained from scratching away the $Cs_{0.7}DMA_{0.3}PbI_3$ films and dissolving it in dimethyl sulfoxide-d_6 (DMSO-d_6) (Fig. 2e). The signals of $-NH_2^+-$ (singlet) and $-CH_3$ (doublet) protons are located at

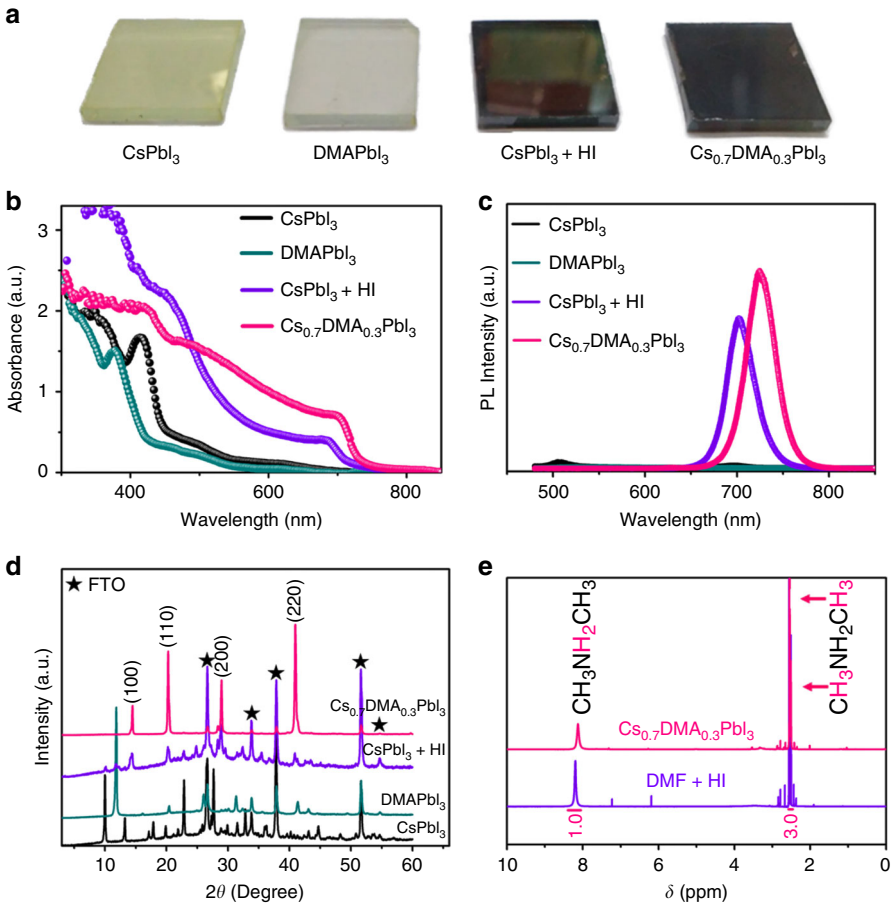

Fig. 2 Film properties and component studies. **a** Photographs, **b** UV-vis absorption spectra, **c** PL spectra, and **d** XRD patterns of a pure $CsPbI_3$ film, a pure $DMAPbI_3$ film, a HI-treated $CsPbI_3$ film, and a $Cs_{0.7}DMA_{0.3}PbI_3$ film. **e** NMR spectra of the powder obtained from scratching away $Cs_{0.7}DMA_{0.3}PbI_3$ films and DMAI polycrystalline powder synthesized from DMF and HI, which were dissolved in DMSO-d_6

$\delta = 8.17$ ppm and $\delta = 2.55$ ppm, respectively. The ratio integrated from the signals of $-NH_2^+-$ and $-CH_3$ is 1:3, indicating that DMA is protonated. The NMR spectrum of the pure DMAI powder confirms the peak position (Supplementary Fig. 6), thus demonstrating DMA is incorporated in the $CsPbI_3$ structure as would be expected by the $Cs_{0.7}DMA_{0.3}PbI_3$ composition. Remarkably, the NMR spectrum of the DMSO-d_6 solution of the powder obtained from scratching away the $CsPbI_3$ film with HI addition also shows the same two peaks in the 1:3 for $-NH_2^+-$ and $-CH_3$ ratio (Supplementary Fig. 7).

The chemical mechanism and reality of so-called $HPbI_3$. Thus, it transpires from the NMR results that the DMA cation is produced via a side reaction (of DMF with HI) and then gets incorporated in the $CsPbI_3$ films. Since only CsI and PbI_2 were dissolved in the DMF solvent, the only possible source of DMA in the precursor solution is DMF itself, which is known to slowly hydrolyze to DMA and formic acid (HCOOH)[60–65]. Addition of HI significantly accelerates the hydrolysis according to Eq. 1, heavily shifting the equilibrium towards the dissociation products, thus generating significant amounts of DMA in the mixture[66].

$$HCON(CH_3)_2 + HI + H_2O \rightarrow (CH_3)_2NH_2I(DMAI) + HCOOH \quad (1)$$

In order to further demonstrate this reaction, we synthesized the DMAI from the reaction of DMF and HI directly (see Methods). As Fig. 2e illustrate, DMAI can indeed be readily formed by the reaction between DMF and HI, with ^{1}H-NMR spectra and XRD patterns confirming its identity in comparison with the commercial DMAI compound (Supplementary Figs. 6 and 8). Note that the two peaks at $\delta = 7.22$ ppm and $\delta = 6.18$ ppm shown in Fig. 2e are assigned to the $-PH_2-$ protons of hypophosphorous acid (H_3PO_2) which presents as a stabilizer in concentrated HI aqueous solutions. Therefore, this is the reason why ^{1}H-NMR spectra of $Cs_{0.7}DMA_{0.3}PbI_3$, $CsPbI_3$ with HI, DMAI, and DMF + HI samples are identical. Most importantly, it explains why the UV-vis absorption, PL, XRD, and ^{1}H-NMR results between the intentionally made $Cs_{0.7}DMA_{0.3}PbI_3$ film and the DMF derived $CsPbI_3$ with HI addition films are so similar. Note that the red shift (around 20 nm) of PL and UV-vis spectra of $Cs_{0.7}DMA_{0.3}PbI_3$ with respect to the $CsPbI_3$ sample with HI is because the former (which contains significant amounts of DMA) adopts the cubic α-$CsPbI_3$ phase, whereas the latter (containing only small amounts of DMA) stabilizes the orthorhombic γ-phase (as would be expected by the effective tolerance factor discussed above).

The hydrolysis of DMF in the presence of acid such as HI as a film fabrication tool has great implications in the fabrication of perovskite films and solar cells. Since HI addition has been reported to alter the phase transition temperature and improve the film morphology of $MAPbI_3$[67], and also was identified as the critical reagent for stabilizing the perovskite phase of $CsPbI_3$, the nature and exact composition of these crystalline films will need to be re-examined[18,25,26,59]. In addition, $HPbI_3$, obtained from

the reaction of HI, DMF, and PbI_2, has been widely used for making stable $FAPbI_3$[38], $CsPbI_3$[31,37,53], and $MAPbI_3$ solar cells[68], which actually does not exist and should be reformulated to $DMAPbI_3$. It is confirmed by the XRD patterns of our $DMAPbI_3$ film (Fig. 2d and Supplementary Fig. 2) and the reported $HPbI_3$[38], showing the exact same reflections. Given that the use of $HPbI_3$ in a serendipitous manner, these systems also need to be revisited and studied carefully under the understanding of the DMF hydrolysis mechanism. It is important to re-evaluate these systems counting the time as a synthetic parameter since the preparation will significantly vary over time as different amounts of DMA are produced at different times of the reactions and therefore the composition of the films will vary accordingly.

In a previous report, we demonstrated that HI addition can alter the $MAPbI_3$ phase transition temperature[67]. A room temperature phase transition from tetragonal to cubic was observed for $MAPbI_3$ films treated with high HX (X = Cl, Br, I) concentrations. In our original hypothesis, we and others speculated that the reduction of the crystallite size induced by the acid were responsible for this phase transition[18,67]. HI can improve the perovskite film morphology and eliminate the hysteresis of $MAPbI_3$ solar cells[69,70]. However, in light of the results reported here, we can now revise our original concept and ascribe the compositional phase transition to the presence of DMA, induced by the presence of acid. Note that the concept of the role of acid expands beyond the HX acids, as other acids such as H_3PO_2[71] appear to have a similar effect. Therefore, based on the above results, all those compositionally-induced phase transitions may be attributed to the introduction of the in-situ forming DMA cation in the perovskite lattice and it applies equally well in the $MAPbI_3$ and $CsPbI_3$ systems. Note that $FAPbI_3$ is excluded since FA is already too large to stabilize the perovskite structure.

Now that we have established that the so-called all-inorganic $CsPbI_3$ films processed with HI and $HPbI_3$ are in fact $Cs_{1-x}DMA_xPbI_3$ films, we return to the study of the latter and their behavior and performance in complete solar cells. The $CsPbI_3$ film with HI addition was prepared by a conventional one-step method and using DMF as solvent[18], actually is unintentionally-made $Cs_{1-x}DMA_xPbI_3$ but we still referred it as HI-treated $CsPbI_3$ in the following discussion. A small amount of HI aqueous solution was added into the $CsPbI_3$ precursor after all materials were dissolved in DMF solvent. All other intentionally-made $Cs_{1-x}DMA_xPbI_3$ ($x = 0$ to 0.5) films were fabricated by CsI, PbI_2, and pre-synthesized DMAI using a solvent-engineering method[14,72] with a mixture of DMF and DMSO as the solvent. Scanning electron microscopy (SEM) images show that the yellow-phase $CsPbI_3$ film has a rough surface with big grains and pin-holes, Fig. 3a. The morphology of the neat yellow $DMAPbI_3$ film is even worse, showing some long and big cracks (Fig. 3b). Fig. 3c shows the one-step method prepared $CsPbI_3$ film treated with HI which clearly has much smoother surface, still containing some pin holes. The best film quality was obtained from the $CsPbI_3$ film with DMA cation i.e., $Cs_{0.7}DMA_{0.3}PbI_3$. As shown in Fig. 3d, the $Cs_{0.7}DMA_{0.3}PbI_3$ film has a smooth surface, big grains and few pinholes. The average grain size of the $Cs_{0.7}DMA_{0.3}PbI_3$ film is around 500 nm, which is comparable with the film thickness. This is desirable since big grains facilitate charge transfer and reduce the recombination at grain boundaries[14]. Fig. 3e shows a cross-sectional SEM of a complete device based on the $Cs_{0.7}DMA_{0.3}PbI_3$ absorber. The 380 nm thick $Cs_{0.7}DMA_{0.3}PbI_3$ film is sandwiched between a thin poly(3,4-ethylenedioxythiophene) polystyrene sulfonate (PEDOT:PSS) hole transporting layer and a thin fullerene (C_{60}) electron transporting layer. The ultra-smooth $Cs_{0.7}DMA_{0.3}PbI_3$ film enables the fabrication of solar cells with an inverted planar structure.

Effects of DMA cation on solar cell performance. We then investigated the effects of various absorbers on device performance. Fig. 4a shows the photocurrent density-voltage (J–V) curves of the representative solar cells based on the yellow $CsPbI_3$, the pale-yellow $DMAPbI_3$, the black HI-treated $CsPbI_3$, and the black $Cs_{0.7}DMA_{0.3}PbI_3$ absorbers, measured under a reverse voltage scan. The performance of the solar cells based on different absorbers shows huge difference. As expected, the solar cells with yellow $CsPbI_3$ and $DMAPbI_3$ absorbers show very poor efficiencies. As shown in Fig. 4a, the solar cell employed the yellow $CsPbI_3$ film achieved a very low PCE of 0.002% with an open-circuit voltage (V_{oc}) of 0.05 V, a short-circuit current density (J_{sc}) of 0.21 mA cm^{-2}, a fill factor (FF) of 22.63%. A similarly low PCE of 0.001% with a V_{oc} of 0.03 V, a J_{sc} of 0.30 mA cm^{-2}, and an FF of 14.23% was obtained for the solar cell employing the yellow $DMAPbI_3$ film. Both $CsPbI_3$ and $DMAPbI_3$ devices were almost short-circuited, due to the poor film quality, non-perovskite structure, and limited light absorption due to their wide band gaps. The device performance of the so-called black $CsPbI_3$ was significantly enhanced after adding HI into the perovskite precursor. The HI-treated $CsPbI_3$ solar cell achieved a V_{oc} of 0.82 V, a J_{sc} of 9.56 mA cm^{-2}, an FF of 61.56%, and a PCE of 4.84%, which is comparable with other reports[18,31]. The enhanced performance can be mainly attributed to the better morphology and the unintended incorporation of DMA cation which can stabilize the $Cs_{1-x}DMA_xPbI_3$ perovskite as a black phase. Nevertheless, adding HI into the perovskite precursor makes it difficult to control the amount of DMA in the final film in a consistent manner, so after realizing the role of HI in the film formation the main focus was given in the easily reproducible fabrication of devices containing controlled amounts of DMA. As expected, the solar cells based on the designed $Cs_{0.7}DMA_{0.3}PbI_3$ absorber yielded much better performance. A significantly enhanced PCE of 10.39% with a high V_{oc} of 1.03 V, a J_{sc} of 15.43 mA cm^{-2}, an FF of 65.61% was achieved for an optimized device, with both the high-quality of the films and narrow band gap contributing to the decent performance of the $Cs_{0.7}DMA_{0.3}PbI_3$ solar cells.

We find that the amount of DMA cation incorporated in the perovskite structure of $CsPbI_3$ has a huge effect on the material properties. Unlike the HI addition to DMF which results in the uncontrollable generation of DMA, it is easy to fabricate $Cs_{1-x}DMA_xPbI_3$ films using precise DMA ratios. First, the film morphology was affected by different amounts of DMA. As shown in Supplementary Fig. 9, $Cs_{0.8}DMA_{0.2}PbI_3$, $Cs_{0.7}DMA_{0.3}PbI_3$, $Cs_{0.6}DMA_{0.4}PbI_3$, and $Cs_{0.5}DMA_{0.5}PbI_3$ films show different morphology. All films are compact and have smooth surface with $Cs_{0.7}DMA_{0.3}PbI_3$ film having the biggest grains. The $Cs_{0.6}DMA_{0.4}PbI_3$, and $Cs_{0.5}DMA_{0.5}PbI_3$ films are compact and have smaller grains. In addition, these films show similar band baps and PL peaks but different absorption intensities (Supplementary Fig. 10). In particular, the $Cs_{0.7}DMA_{0.3}PbI_3$ film shows the strongest absorption at long wavelength range. Supplementary Fig. 11 shows that the different films also have different XRD results. The diffraction intensities of the cubic $Cs_{0.6}DMA_{0.4}PbI_3$ and $Cs_{0.5}DMA_{0.5}PbI_3$ films are weaker while the extra peak at $2\theta = 11.8°$ indicates that $DMAPbI_3$ is present as a second phase, suggesting that the substitution of DMA for Cs is limited. $Cs_{0.7}DMA_{0.3}PbI_3$ and $Cs_{0.8}DMA_{0.2}PbI_3$ show the exclusive formation of the black α-$CsPbI_3$ phase along with the former orienting preferentially along both (100) and (110) planes and the latter exclusively along the (110) planes. From the combined data, around 30% of DMA seems to be the optimum amount to make high-quality perovskite film. This is also reflected in the device performance of the corresponding solar cells based on the $CsPbI_3$ absorbers with various amounts of DMA. Supplementary Fig. 12 shows the J–V curves of the solar

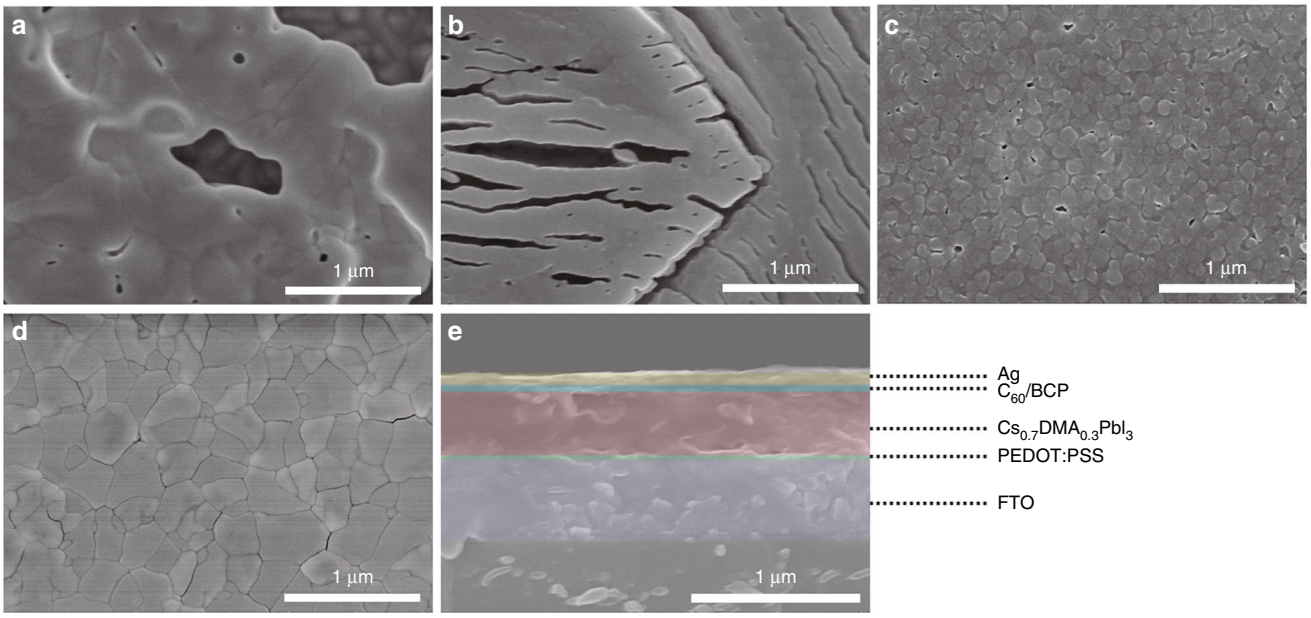

Fig. 3 Film and device morphology. Top view SEM images of **a** a $CsPbI_3$, **b** a $DMAPbI_3$, **c** a HI-treated $CsPbI_3$, and **d** a $Cs_{0.7}DMA_{0.3}PbI_3$ film deposited on FTO/PEDOT substrates. **e** Cross-sectional SEM image of a completed device using a PEDOT:PSS hole transporting layer, a $Cs_{0.7}DMA_{0.3}PbI_3$ absorber, a C_{60}/BCP electron transporting layer, and a Ag metal electrode

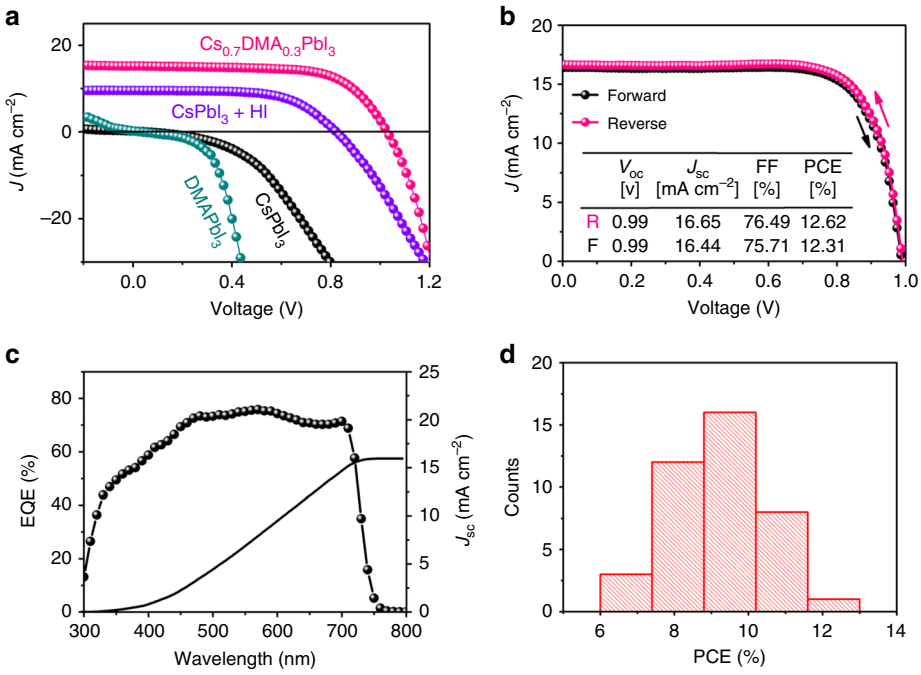

Fig. 4 Solar cell performance. **a** *J*–*V* curves of devices using various absorbers measured under reverse voltage scans (from V_{oc} to 0 V). **b** *J*–*V* curves of the champion $Cs_{0.7}DMA_{0.3}PbI_3$ solar cell measured under different voltage scan directions. **c** EQE spectrum and integrated J_{sc} of a $Cs_{0.7}DMA_{0.3}PbI_3$ solar cell. **d** PCE statistics for 40 $Cs_{0.7}DMA_{0.3}PbI_3$ solar cells

cells using the $Cs_{0.8}DMA_{0.2}PbI_3$, $Cs_{0.7}DMA_{0.3}PbI_3$, $Cs_{0.6}DMA_{0.4}PbI_3$, and $Cs_{0.5}DMA_{0.5}PbI_3$ absorbers. The device performance first increases and then decreases as the DMA amount increases. As expected, the solar cell derived from the best-quality $Cs_{0.7}DMA_{0.3}PbI_3$ film achieved the highest performance (Supplementary Table 1).

Figure 4b shows the *J*–*V* curves of the best-performing $Cs_{0.7}DMA_{0.3}PbI_3$ solar cell measured under different voltage scan directions. This solar cell achieved a V_{oc} of 0.99 V, a J_{sc} of 16.65 mA cm^{-2}, an FF of 76.49%, and therefore a high PCE of 12.62% when measured under the reverse voltage scan. A similar PCE of 12.31% with a V_{oc} of 0.99 V, a J_{sc} of 16.44 mA cm^{-2}, and an FF of 75.71% was achieved for the solar cell measured under the forward voltage scan, suggesting small hysteresis behavior of our devices. External quantum efficiency (EQE) measurement was taken to confirm the high J_{sc} obtained from the *J*–*V* curves. The EQE spectrum of the solar cell based on the $Cs_{0.7}DMA_{0.3}PbI_3$ absorber is shown in Fig. 4c. The cell shows

high average value in the whole visible wavelength range. The J_{sc} integrated from the EQE curve is about 15.95 mA cm^{-2}, which is very close to the J_{sc} measured from the J–V curves. To check the reproducibility of the device performance, we then made 40 solar cells based on the $Cs_{0.7}DMA_{0.3}PbI_3$ absorbers. The histograms of statistics PCEs for these cells are shown in Fig. 4d, ranged from 6.73 to 12.62% due to the inhomogeneous film morphology. The 40 solar cells achieved an average PCE of 9.27 ± 1.28% with a V_{oc} of 1.01 ± 0.03 V, a J_{sc} of 15.45 ± 1.80 mA cm^{-2}, and an FF of 59.40 ± 4.01%.

Furthermore, we also added the DMA cation into solutions of $CsPbI_2Br$ and $CsPbIBr_2$ perovskites. Supplementary Fig. 13a-b shows UV-vis absorption and XRD pattern of a $Cs_{0.7}DMA_{0.3}I_2Br$ film coated on a FTO/PEDOT:PSS substrate. The $Cs_{0.7}DMA_{0.3}I_2Br$ film shows an absorption onset at around 685 nm, according to a band gap of around 1.8 eV (Supplementary Fig. 13a). The $Cs_{0.7}DMA_{0.3}I_2Br$ film has good crystalline quality and shows peaks at 14.7°, 20.5°, 29.5°, and 41.6° (Supplementary Fig. 13b), which can be indexed to the (100), (110), (200), and (220) planes. Supplementary Fig. 13c shows the J–V curve of a solar cell based on the $CsPbI_2Br$ absorber. The $Cs_{0.7}DMA_{0.3}I_2Br$ solar cell achieved a PCE of 5.24%, a V_{oc} of 1.02 V, a J_{sc} of 12.39 mA cm^{-2}, and an FF of 41.67%. The lower J_{sc} is consistent with the wider band gap compared to $Cs_{0.7}DMA_{0.3}PbI_3$. The $Cs_{0.7}DMA_{0.3}PbIBr_2$ film has a more blue-shifted absorption onset at around 620 nm, according to a wider band gap of around 2.0 eV, Supplementary Fig. 14a. The $Cs_{0.7}DMA_{0.3}PbIBr_2$ solar cell achieved a PCE of 2.80%, a V_{oc} of 1.11 V, a J_{sc} of 8.55 mA cm^{-2}, and an FF of 29.57% (Supplementary Fig. 14c). A much lower J_{sc} is obtained from the $Cs_{0.7}DMA_{0.3}PbIBr_2$ cell because of the much wider band gap. Higher performance for the $Cs_{1-x}DMA_xPbI_2Br$ and $Cs_{1-x}DMA_xPbIBr_2$ cells is anticipated after further device optimization.

Discussion

We have demonstrated that small cation DMA can be formed in suite by the HI induced decomposition of DMF and can subsequently stabilize the black perovskite phase of $CsPbI_3$. However, the films are not really the all-inorganic $CsPbI_3$ phase but the $Cs_{1-x}DMA_xPbI_3$ ($x = 0.2$ to 0.5) cubic perovskite solid solution. $Cs_{0.7}DMA_{0.3}PbI_3$ has a band gap of around 1.7 eV and can enable high efficiency solar cells. In the context of this work, we realize that DMA is likely present in many other devices reported in the past, since it can be inadvertently created from the degradation of the commonly used DMF solvent and then incorporated to some extend in the perovskite structures as an A cation. This DMF decomposition process is accelerated by acidic hydrolysis, and must be taken into account when considering the role of the solvent degradation in device performance. DMF hydrolysis therefore explains the effects of the widely used HI addition and $HPbI_3$ methods to stabilize the purported all-inorganic black $CsPbI_3$ perovskite. Based on above results, we show that $HPbI_3$ does not exist while at the same time it is actual in situ formation of the DMA cation, which should widely exist in the perovskites processed with DMF, HI, and $HPbI_3$. We anticipate that the DMA cation, which now has been revealed as a viable A-site cation, may be unsuspectingly occurring not only in "$CsPbI_3$ films" but also in films of other perovskite families, for example, pure MA, MA/FA, Cs/FA, and Cs/MA/FA mixed-cation perovskites. We suggest that NMR spectroscopy be used for such films by dissolving them in pure DMF or DMSO to check for the presence of the DMA cation.

Methods

Device fabrication. For the DMAI synthesis, DMF was slowly added into the HI solution with continue stirring at 0 °C for 30 min. Water and excess DMF in solution was removed by low-vacuum rotary evaporation and then a white polycrystalline powder (DMAI powder) was obtained. Pre-cleaned FTO substrates were treated with UV-Ozone for 30 min. PEDOT:PSS films were coated on the FTO substrates with a spin-rate of 4000 rpm for 30 s and then annealing for 30 min at 150 °C. Perovskite films were deposited on FTO/PEDOT:PSS substrates in a N_2-filled glovebox. Neat $CsPbI_3$, neat $DMAPbI_3$, and $Cs_{1-x}DMA_xPbX_3$ (X = I, Br) films were prepared by a solvent-engineering method[14] at a spin rate of 4000 rpm for 60 s. 0.7 ml of diethyl ether was quickly dropped onto the rotating substrates during the spin-coating process. $CsPbI_3$ films with HI addition were prepared by a one-step method at a spin rate of 2000 rpm for 60 s[18]. The neat $CsPbI_3$ precursor was prepared by dissolving 260 mg of CsI (99.999%, Sigma-Aldrich) and 461 mg of PbI_2 (beads, 99.999%, Sigma-Aldrich) in 0.8 ml of DMF (anhydrous, 99.8%, Sigma-Aldrich) and 0.2 ml of DMSO (anhydrous,≥ 99.9%, Sigma-Aldrich). The neat $DMAPbI_3$ precursor was prepared by dissolving 173 mg of DMAI and 461 mg of PbI_2 in 0.8 ml of DMF and 0.2 ml of DMSO. The $Cs_{1-x}DMA_xPbI_3$ precursor was prepared by dissolving $(1-x) \times 260$ mg of CsI, $x \times 173$ mg of DMAI, and 461 mg of PbI_2 in 0.8 ml of DMF and 0.2 ml of DMSO. The $CsPbI_3$ precursor with HI addition was prepared by dissolving 260 mg of CsI and 461 mg of PbI_2 in 2 ml of DMF and then adding 3.3 vol% HI (57 wt.% in H_2O, 99.95%, Sigma-Aldrich) into the dissolved solution. All the films were annealed for 2 min at 60 °C and then 5 min at 100 °C on a hot plate. To complete the devices, a thin C_{60} (20 nm), a thin 2,9-dimethyl-4,7-diphenyl-1,10-phenanthroline (BCP) (5 nm), and a Ag (80 nm) films were sequentially thermal evaporated on top of the absorber layers using a metal mask. The active area of the solar cells was 0.09 cm^2.

Film and device characterization. ^{1}H-NMR spectra were measured with Bruker Avance III 600 MHz system with BBI probe. The morphology of the films and devices was examined on a high-resolution field emission SEM (Hitachi SU8030). XRD patterns of the films were characterized by a Rigaku Miniflex600 pXRD (Cu Kα graphite, $\lambda = 1.5406$ Å) operating at 40 kV/15 mA with a Kβ foil filter. PL spectra were taken on a Horiba LabRAM HR Evolution confocal Raman microscope spectrometer (600 g mm^{-1} diffraction grating) equipped with a diode continuouswave laser (473 nm, 25 mW) and a Synapse charge-coupled device camera. UV-vis absorption spectra of the films were measured with a Shimadzu UV-3600 UV-vis NIR spectrometer operating in the 200–2000 nm region at room temperature. EQE spectrum was obtained on an Oriel model QE-PV-SI instrument equipped with a NIST-certified Si diode. J–V curves were recorded using a Keithley model 2400 instrument under AM1.5 G simulated irradiation with a standard solar simulator (Abet Technologies). J–V curves were measured from 1.5 V to −0.2 V (reverse) or from −0.2 V to 1.5 V (forward) with an integration time of 16.67 ms and a voltage step of 11.4 mV. The light intensity of the solar simulator was calibrated by a NREL-certified monocrystalline silicon solar cell.

Data availability

The authors declare that the main data supporting the findings of this study are available within the article and its Supplementary Information. Extra data are available from the authors upon request.

Received: 11 September 2018 Accepted: 16 October 2018
Published online: 14 November 2018

References

1. Mitzi, D. B. Synthesis, structure, and properties of organic-inorganic perovskites and related materials. *Prog. Inorg. Chem.* **48**, 1–121 (1999).
2. Yin, W. J., Shi, T. & Yan, Y. Unique properties of halide perovskites as possible origins of the superior solar cell performance. *Adv. Mater.* **26**, 4653–4658 (2014).
3. Dong, Q. et al. Electron-hole diffusion lengths>175 μm in solution-grown CH3NH3PbI3 single crystals. *Science* **347**, 967–970 (2015).
4. Stranks, S. D. et al. Electron-hole diffusion lengths exceeding 1 micrometer in an organometal trihalide perovskite absorber. *Science* **342**, 341–344 (2013).
5. Stoumpos, C. C., Malliakas, C. D. & Kanatzidis, M. G. Semiconducting tin and lead iodide perovskites with organic cations: phase transitions, high mobilities, and near-infrared photoluminescent properties. *Inorg. Chem.* **52**, 9019–9038 (2013).
6. Nagabhushana, G. P., Shivaramaiah, R. & Navrotsky, A. Thermochemistry of multiferroic organic-inorganic hybrid perovskites $[(CH_3)_2NH_2][M(HCOO)_3]$ (M = Mn, Co, Ni, and Zn). *J. Am. Chem. Soc.* **137**, 10351–10356 (2015).
7. Ke, W., Stoumpos, C. C. & Kanatzidis, M. G. "Unleaded" perovskites: status quo and future prospects of tin-based perovskite solar cells. *Adv. Mater.* 1803230. https://doi.org/10.1002/adma.201803230 (2018).
8. Ke, W. et al. Enhanced photovoltaic performance and stability with a new type of hollow 3D perovskite {en}$FASnI_3$. *Sci. Adv.* **3**, e1701293 (2017).
9. Li, X. et al. A vacuum flash–assisted solution process for high-efficiency large-area perovskite solar cells. *Science* **353**, 58–62 (2016).
10. Kim, H. S. et al. Lead iodide perovskite sensitized all-solid-state submicron thin film mesoscopic solar cell with efficiency exceeding 9%. *Sci. Rep.* **2**, 591 (2012).

11. Lee, M. M., Teuscher, J., Miyasaka, T., Murakami, T. N. & Snaith, H. J. Efficient hybrid solar cells based on meso-superstructured organometal halide perovskites. *Science* **338**, 643–647 (2012).
12. Yang, W. S. et al. Iodide management in formamidinium-lead-halide–based perovskite layers for efficient solar cells. *Science* **356**, 1376–1379 (2017).
13. Saliba, M. et al. Incorporation of rubidium cations into perovskite solar cells improves photovoltaic performance. *Science* **354**, 206–209 (2016).
14. Ke, W. et al. Employing lead thiocyanate additive to reduce the hysteresis and boost the fill factor of planar perovskite solar cells. *Adv. Mater.* **28**, 5214–5221 (2016).
15. Ke, W. et al. Low-temperature solution processed tin oxide as an alternative electron transporting layer for efficient perovskite solar cells. *J. Am. Chem. Soc.* **137**, 6730–6733 (2015).
16. Gao, L.-L., Li, C.-X., Li, C.-J. & Yang, G.-J. Large-area high-efficiency perovskite solar cells based on perovskite films dried by the multi-flow air knife method in air. *J. Mater. Chem. A* **5**, 1548–1557 (2017).
17. Chen, H. et al. Inorganic perovskite solar cells: a rapidly growing field. *Sol. RRL* **2**, 1700188 (2018).
18. Eperon, G. E. et al. Inorganic caesium lead iodide perovskite solar cells. *J. Mater. Chem. A* **3**, 19688–19695 (2015).
19. Liang, J., Liu, J. & Jin, Z. All-inorganic halide perovskites for optoelectronics: progress and prospects. *Solar RRL* **1**, 1700086 (2017).
20. Nagabhushana, G. P., Shivaramaiah, R. & Navrotsky, A. Direct calorimetric verification of thermodynamic instability of lead halide hybrid perovskites. *Proc. Natl Acad. Sci. USA* **113**, 7717–7721 (2016).
21. Marronnier, A. et al. Anharmonicity and disorder in the black phases of cesium lead iodide used for stable inorganic perovskite solar cells. *ACS Nano* **12**, 3477–3486 (2018).
22. Sutton, R. J. et al. Cubic or orthorhombic? Revealing the crystal structure of metastable black-phase $CsPbI_3$ by theory and experiment. *ACS Energy Lett.* **3**, 1787–1794 (2018).
23. Chung, I. et al. $CsSnI_3$: Semiconductor or metal? High electrical conductivity and strong near-infrared photoluminescence from a single material. High hole mobility and phase-transitions. *J. Am. Chem. Soc.* **134**, 8579–8587 (2012).
24. Lau, C. F. J. et al. Strontium-doped low-temperature-processed $CsPbI_2Br$ perovskite solar cells. *ACS Energy Lett.* **2**, 2319–2325 (2017).
25. Hu, Y. et al. Bismuth incorporation stabilized α-$CsPbI_3$ for fully inorganic perovskite solar cells. *ACS Energy Lett.* **2**, 2219–2227 (2017).
26. Luo, P. et al. Solvent engineering for ambient-air-processed, phase-stable $CsPbI_3$ in perovskite solar cells. *J. Phys. Chem. Lett.* **7**, 3603–3608 (2016).
27. Sanehira, E. M. et al. Enhanced mobility $CsPbI_3$ quantum dot arrays for record-efficiency, high-voltage photovoltaic cells. *Sci. Adv.* **3**, eaao4204 (2017).
28. Swarnkar, A. et al. Quantum dot–induced phase stabilization of α-$CsPbI_3$ perovskite for high-efficiency photovoltaics. *Science* **354**, 92–95 (2016).
29. Frolova, L. A. et al. Highly efficient all-inorganic planar heterojunction perovskite solar cells produced by thermal coevaporation of CsI and PbI_2. *J. Phys. Chem. Lett.* **8**, 67–72 (2017).
30. Wang, Q. et al. Stabilizing the α-phase of $CsPbI_3$ perovskite by sulfobetaine zwitterions in one-step spin-coating films. *Joule* **1**, 371–382 (2017).
31. Zhang, T. et al. Bication lead iodide 2D perovskite component to stabilize inorganic α-$CsPbI_3$ perovskite phase for high-efficiency solar cells. *Sci. Adv* **3**, e1700841 (2017).
32. Wang, Q. et al. μ-Graphene crosslinked $CsPbI_3$ quantum dots for high efficiency solar cells with much improved stability. *Adv. Energy Mater.* **8**, 1800007 (2018).
33. Wang, P. et al. Solvent-controlled growth of inorganic perovskite films in dry environment for efficient and stable solar cells. *Nat. Commun.* **9**, 2225 (2018).
34. Zhao, B. et al. Thermodynamically stable orthorhombic γ-$CsPbI_3$ thin films for high-performance photovoltaics. *J. Am. Chem. Soc.* **140**, 11716–11725 (2018).
35. Wang, Y., Zhang, T., Kan, M. & Zhao, Y. Bifunctional stabilization of all-inorganic α-$CsPbI_3$ perovskite for 17% efficiency photovoltaics. *J. Am. Chem. Soc.* **140**, 12345–12348 (2018).
36. Protesescu, L. et al. Nanocrystals of cesium lead halide perovskites ($CsPbX_3$, X = Cl, Br, and I): novel optoelectronic materials showing bright emission with wide color gamut. *Nano Lett.* **15**, 3692–3696 (2015).
37. Jiang, Y. et al. Reduced-dimensional α-$CsPbX_3$ perovskites for efficient and stable photovoltaics. *Joule* **2**, 1356–1368 (2018).
38. Wang, F., Yu, H., Xu, H. & Zhao, N. $HPbI_3$: a new precursor compound for highly efficient solution-processed perovskite solar cells. *Adv. Funct. Mater.* **25**, 1120–1126 (2015).
39. Kieslich, G., Sun, S. & Cheetham, A. K. Solid-state principles applied to organic-inorganic perovskites: new tricks for an old dog. *Chem. Sci.* **5**, 4712–4715 (2014).
40. Goldschmidt, V. M. Die gesetze der krystallochemie. *Naturwissenschaften* **14**, 477–485 (1926).
41. Stoumpos, C. C. & Kanatzidis, M. G. Halide perovskites: poor man's high-performance semiconductors. *Adv. Mater.* **28**, 5778–5793 (2016).
42. Stoumpos, C. C. & Kanatzidis, M. G. The renaissance of halide perovskites and their evolution as emerging semiconductors. *Acc. Chem. Res.* **48**, 2791–2802 (2015).
43. Møller, C. K. [The structure of perovskite-like caesium plumbo trihalides]. *Mat. Fys. Medd. Dan. Vid. Sels.* **32**, 1–18 (1959).
44. Nam, J. K. et al. Potassium incorporation for enhanced performance and stability of fully inorganic cesium lead halide perovskite solar cells. *Nano. Lett.* **17**, 2028–2033 (2017).
45. Kulbak, M. et al. Cesium enhances long-term stability of lead bromide perovskite-based solar cells. *J. Phys. Chem. Lett.* **7**, 167–172 (2016).
46. Sutton, R. J. et al. Bandgap-tunable cesium lead halide perovskites with high thermal stability for efficient solar cells. *Adv. Energy Mater.* **6**, 1502458 (2016).
47. Ma, Q., Huang, S., Wen, X., Green, M. A. & Ho-Baillie, A. W. Y. Hole transport layer free inorganic $CsPbIBr_2$ perovskite solar cell by dual source thermal evaporation. *Adv. Energy Mater.* **6**, 1502202 (2016).
48. Lau, C. F. J. et al. $CsPbIBr_2$ perovskite solar cell by spray-assisted deposition. *ACS Energy Lett.* **1**, 573–577 (2016).
49. Chang, X. et al. Carbon-based $CsPbBr_3$ perovskite solar cells: all-ambient processes and high thermal stability. *ACS Appl. Mater. Interfaces* **8**, 33649–33655 (2016).
50. Niezgoda, J. S., Foley, B. J., Chen, A. Z. & Choi, J. J. Improved charge collection in highly efficient $CsPbBrI_2$ solar cells with light-induced dealloying. *ACS Energy Lett.* **2**, 1043–1049 (2017).
51. Zeng, Q. et al. Polymer-passivated inorganic cesium lead mixed-halide perovskites for stable and efficient solar cells with high open-circuit voltage over 1.3 V. *Adv. Mater.* **30**, 1705393 (2018).
52. Ma, Q. et al. The effect of stoichiometry on the stability of inorganic cesium lead mixed-halide perovskites solar cells. *J. Phys. Chem. C.* **121**, 19642–19649 (2017).
53. Wang, Y., Zhang, T., Xu, F., Li, Y. & Zhao, Y. A facile low temperature fabrication of high performance $CsPbI_2Br$ all-inorganic perovskite solar cells. *Sol. RRL* **2**, 1700180 (2018).
54. Bian, H. et al. Graded bandgap $CsPbI_{2+x}Br_{1-x}$ perovskite solar cells with a stabilized efficiency of 14.4%. *Joule* **2**, 1500–1510 (2018).
55. Li, Z. et al. Stabilizing perovskite structures by tuning tolerance factor: formation of formamidinium and cesium lead iodide solid-state alloys. *Chem. Mater.* **28**, 284–292 (2015).
56. Stoumpos, C. C., Mao, L., Malliakas, C. D. & Kanatzidis, M. G. Structure-band gap relationships in hexagonal polytypes and low-dimensional structures of hybrid tin iodide perovskites. *Inorg. Chem.* **56**, 56–73 (2017).
57. Kieslich, G., Sun, S. & Cheetham, A. K. Solid-state principles applied to organic–inorganic perovskites: new tricks for an old dog. *Chem. Sci.* **5**, 4712–4715 (2014).
58. Mancini, A. et al. Synthesis, structural and optical characterization of $APbX_3$ (A = methylammonium, dimethylammonium, trimethylammonium; X = I, Br, Cl) hybrid organic-inorganic materials. *J. Solid State Chem.* **240**, 55–60 (2016).
59. Kim, Y. G. et al. Cesium lead iodide solar cells controlled by annealing temperature. *Phys. Chem. Chem. Phys.* **19**, 6257–6263 (2017).
60. Muzart, J. N,N-Dimethylformamide: much more than a solvent. *Tetrahedron* **65**, 8313–8323 (2009).
61. Juillard, J. Dimethylformamide: purification, tests for purity and physical properties. *Pure Appl. Chem.* **49**, 885–892 (1977).
62. Noel, N. K. et al. Unveiling the influence of pH on the crystallization of hybrid perovskites, delivering low voltage loss photovoltaics. *Joule* **1**, 328–343 (2017).
63. Dou, B. et al. Degradation of highly alloyed metal halide perovskite precursor inks: mechanism and storage solutions. *ACS Energy Lett.* **3**, 979–985 (2018).
64. Nayak, P. K. et al. Mechanism for rapid growth of organic-inorganic halide perovskite crystals. *Nat. Commun.* **7**, 13303 (2016).
65. Spanopoulos, I. et al. Enhanced gas-sorption properties of a high surface area, ultramicroporous magnesium formate. *CrystEngComm* **17**, 532–539 (2015).
66. Jain, P., Dalal, N. S., Toby, B. H., Kroto, H. W. & Cheetham, A. K. Order−disorder antiferroelectric phase transition in a hybrid inorganic−organic framework with the perovskite architecture. *J. Am. Chem. Soc.* **130**, 10450–10451 (2008).
67. Soe, C. M. et al. Room temperature phase transition in methylammonium lead iodide perovskite thin films induced by hydrohalic acid additives. *ChemSusChem* **9**, 2656–2665 (2016).
68. Pang, S. et al. Transformative evolution of organolead triiodide perovskite thin films from strong room-temperature solid-gas interaction between $HPbI_3$-CH_3NH_2 precursor pair. *J. Am. Chem. Soc.* **138**, 750–753 (2016).
69. Heo, J. H., Han, H. J., Kim, D., Ahn, T. K. & Im, S. H. Hysteresis-less inverted $CH_3NH_3PbI_3$ planar perovskite hybrid solar cells with 18.1% power conversion efficiency. *Energy Environ. Sci.* **8**, 1602–1608 (2015).
70. Heo, J. H. et al. Planar $CH_3NH_3PbI_3$ perovskite solar cells with constant 17.2% average power conversion efficiency irrespective of the scan rate. *Adv. Mater.* **27**, 3424–3430 (2015).
71. Xiao, Z. et al. Unraveling the hidden function of a stabilizer in a precursor in improving hybrid perovskite film morphology for high efficiency solar cells. *Energy Environ. Sci.* **9**, 867–872 (2016).

72. Jeon, N. J. et al. Solvent engineering for high-performance inorganic–organic hybrid perovskite solar cells. *Nat. Mater.* **13**, 897–903 (2014).

Acknowledgements

This work was supported in part by the LEAP Center, an Energy Frontier Research Center funded by the U.S. Department of Energy, Office of Science, and Office of Basic Energy Sciences under Award DE-SC0001059 (solar cell fabrication and characterization). Work in sample synthesis, processing and structural characterization was supported by grant Department of Energy, Office of Science grant SC0012541. This work made use of the EPIC facility (NUANCE Center-Northwestern University), which has received support from the MRSEC program (NSF DMR-1720139) at the Materials Research Center, and the Nanoscale Science and Engineering Center (EEC-0118025/003), both programs of the National Science Foundation; the State of Illinois; and Northwestern University.

Author contributions

W.K., C.C.S., and M.G.K. conceived the idea, designed the experiments, and wrote the manuscript. I.S. performed the NMR measurements and analyzed the data. W.K. carried out film and device fabrication and characterization. All authors discussed the results and commented on the manuscript. M.G.K. supervised the project.

Additional information

Supplementary Information accompanies this paper at https://doi.org/10.1038/s41467-018-07204-y.

Competing interests: The authors declare no competing interests.